chemosensors

MDPI

Article

Chemoresistive Properties of V_2CT_x MXene and the V_2CT_x/V_3O_7 Nanocomposite Based on It

Artem S. Mokrushin [1,*], Ilya A. Nagornov [1], Aleksey A. Averin [2], Tatiana L. Simonenko [1], Nikolay P. Simonenko [1], Elizaveta P. Simonenko [1] and Nikolay T. Kuznetsov [1]

1 Kurnakov Institute of General and Inorganic Chemistry of the Russian Academy of Sciences, 31 Leninsky pr., Moscow 119991, Russia
2 Frumkin Institute of Physical Chemistry and Electrochemistry, Russian Academy of Sciences, 31 Leninsky pr., bldg. 4, Moscow 199071, Russia
* Correspondence: artyom.nano@gmail.com

Abstract: The *in-situ* Raman spectroscopy oxidation of the accordion-like V_2CT_x MXene has been studied. It was found that a nanocomposite of V_2CT_x/V_3O_7 composition was formed as a result. The elemental and phase composition, the microstructure of the synthesized V_2CT_x powder and MXene film as well as the V_2CT_x/V_3O_7 nanocomposite obtained at a minimum oxidation temperature of 250 °C were studied using a variety of physical and chemical analysis methods. It was found that the obtained V_2CT_x and V_2CT_x/V_3O_7 films have an increased sensitivity to ammonia and nitrogen dioxide, respectively, at room temperature and zero humidity. It was shown that the V_2CT_x/V_3O_7 composite material is characterized by an increase in the response value for a number of analytes (including humidity) by more than one order of magnitude, as well as a change in their detection mechanisms compared to the individual V_2CT_x MXene.

Keywords: MXene; chemoresistive gas sensors; V_2C; vanadium oxide; Raman; 2D-nanomaterials

Citation: Mokrushin, A.S.; Nagornov, I.A.; Averin, A.A.; Simonenko, T.L.; Simonenko, N.P.; Simonenko, E.P.; Kuznetsov, N.T. Chemoresistive Properties of V_2CT_x MXene and the V_2CT_x/V_3O_7 Nanocomposite Based on It. *Chemosensors* **2023**, *11*, 142. https://doi.org/10.3390/chemosensors11020142

Academic Editors: Kai Xu and Zhong Li

Received: 5 January 2023
Revised: 6 February 2023
Accepted: 13 February 2023
Published: 15 February 2023
Corrected: 4 December 2023

1. Introduction

The family of two-dimensional (2D) transition d-metal carbides with the general formula $M_{n+1}C_nT_x$ has attracted the attention of the scientific community in recent years due to its unique properties and high variability of the surface chemistry [1,2]. Currently, the most studied MXenes are the Ti_2CT_x and $Ti_3C_2T_x$ carbide compounds to which the vast majority of the work has been devoted [3–6]. However, there are more and more studies devoted to other two-dimensional transition metal carbides, including Mo_2CT_x, Nb_2CT_x, V_2CT_x [7–10] and various nanocomposites based on them [11–14], are also emerging. At the moment, researchers continue to search and find different ways to synthesize and apply MXenes. The vast majority of works on V_2CT_x are devoted to their use in the composition of lithium-ion batteries and supercapacitors [15–17]. V_2CT_x MXene is also used in ferromagnetics [18], antibacterial coatings [19], memristors [20], hydrogen storage devices [21], in catalysis during the oxygen evolution reaction (OER) [22], as well as in chemoresistive gas sensors [23].

The strong interactions of gases with the surface of MXenes corresponding to high negative adsorption energies (as confirmed by DFT calculations) allow this class of compounds to be successfully used as a sensitive materials in chemoresistive gas sensors [24,25]. The mixed and metallic conductivity of individual MXenes allows for obtaining responses at room temperature with a high signal-to-noise ratio (SNR) [26], which distinguishes them from metal oxide semiconductors (MOS), the classical receptor materials for chemoresistive gas sensors [27–30].

For V_2CT_x MXene, there is sporadic work in the literature on its use in the composition of chemoresistive gas sensors. In [31] the responses to various gases capable of hydrogen bonding (NH_3, triethylamine, ethanol, methanol, acetone, and formaldehyde) were studied

depending on the type of etching agent. It has been shown that after the synthesis, the surface functionalization of V_2CT_x MXenes changes and different types of responses (so-called *n*- and *p*-type, which correspond to the decrease and increase in electrical resistance when the analyte is injected) to the same gases are observed. In [32], for the obtained V_2CT_x MXene, the authors managed to fix the response to 5–50 ppm NO_2; however, data on the responses to other gases are not given, which makes it difficult to assess the selectivity of the obtained MXene. In [33], Eunji Lee et al. carried out a comprehensive study of the gas-sensitive chemoresistive properties of V_2CT_x MXenes, and found that the greatest response of a large number of analyzed gases was obtained for hydrogen. Xingwei Wang et al. [34] described a synergistic process to fabricate a supercapacitor and simultaneously a gas sensor for ammonia based on a polyaniline/V_2C MXene composite with autonomous power supply from an electromagnetic–triboelectric hybrid generator. The authors were able to obtain responses of 0.3–10 ppm NH_3 at 20 °C with high selectivity. The described approach is extremely promising and state-of-the-art.

The use of MXenes as sensitive materials at room temperatures is due to the fact that they are prone to oxidation at increasing operating temperatures in an air atmosphere. In [35], using TG/DTA and XRD analyses it was shown that V_2CT_x MXene is completely oxidized to V_2O_5 at temperatures above 500 °C. The thermograms presented in the article show an intense exothermic effect with a maximum at 332 °C, accompanied by an increase in mass, when heating the MXenes in an air atmosphere, which is associated with the oxidation process of the MXenes. Unfortunately, the authors did not present data on the phase composition of oxidized MXene in the specified temperature range, which complicates the interpretation of the given data. In [36] the authors studied in situ changes in the phase composition of V_2CT_x MXene in different gas environments using Raman spectroscopy. According to the data obtained, it can be seen that in the air atmosphere the oxidation of MXene begins around 400 °C. Such studies are extremely important for fine control of the phase composition in the context of obtaining V_2CT_x/VO_x nanocomposites for various applications, including chemical gas sensing.

Previously, we have obtained titanium carbide MXenes [37,38], and studied the phase transformation of the Ti_2CT_x MXenes film using in situ Raman spectroscopy and studied the effect of the oxidation process on its chemoresistive properties [39]. The chemoresistive properties of the complex vanadium–titanium carbide $Ti_{0.2}V_{1.8}C$ have also been previously studied [40]. The present work is devoted to the study of the oxidation process of V_2CT_x MXene film using in situ Raman spectroscopy and to the study of the gas-sensitive chemoresistive properties of the obtained nanomaterial to a wide group of analyte gases.

2. Materials and Methods

2.1. Synthesis and Application

Reagents: vanadium metal powders (99.9%, 0.5–100 μm, Ruskhim, Moscow, Russia), aluminum (99.2%, 30 μm, Ruskhim, Moscow, Russia), graphite (MPG-8 grade, Ruskhim, Moscow, Russia), potassium bromide KBr (99%, Ruskhim, Moscow, Russia), sodium fluoride NaF (>99%, Reahim, Moscow, Russia), hydrofluoric acid (50%, Honeywell International Inc, Charlotte, NC, USA), hydrochloric acid (36%, Sigma Tek, Moscow, Russia).

The synthesis of V_2CT_x MXene was carried out by selective etching of aluminum contained in the MAX-phase of V_2AlC under the influence of hydrofluoric and hydrochloric acid solutions. Methods for the synthesis of V_2AlC and V_2CT_x, which are close to those used in this work, are described in detail in [40]. Briefly, to obtain V_2AlC powders of aluminum, vanadium, graphite and potassium bromide were mixed in the ratios n(V):n(Al):n(C) = 2:1.2:0.8 and m(V + Al + C) = m(KBr), co-milled, compacted into tablets and subjected to heat treatment in a muffle furnace at 1000 °C [39,40].

To obtain an accordion-like V_2CT_x MXene, a 1 g MAX-phase V_2AlC sample was usually typically added to a solution containing 12 mL of HF (50%) and 8 mL of HCl (36%). After stirring at room temperature for 30 min, the system was heated to 40 ± 5 °C and kept under these conditions under stirring for 120 h. The resulting powder was separated

by centrifugation and washed repeatedly with distilled water until pH ~5–6. The sample was then washed twice with ethanol and centrifuged again. The resulting precipitate was redispersed in ethanol in an ultrasonic bath for 30 min, most of the impurities (primarily MAX-phase particles) were separated by centrifugation of the dispersion at 1000 rpm for 5 min. The dispersion of MXene in ethanol was evaporated, and the resulting phase was dried in a vacuum at 150 °C.

The MXene receptor layer was deposited on a special Al_2O_3 substrate with platinum interdigital electrodes and a heater (on the reverse side) by microextrusion printing (10 μm resolution) using a three-coordinate positioning system equipped with a pneumatic and capillary dispenser in the form of a hollow needle with an internal diameter of 150 μm. A dispersion of V_2CT_x MXene in butanol with a concentration of ~5 mg/mL was used. The coating was dried in a desiccator and then held in a vacuum at 150 °C for 5 min.

2.2. Instrumentation

Micrographs and the chemical composition of the surface of the samples were obtained by scanning (NVision 40 scanning electron microscope, Carl Zeiss, (Oberkochen, Germany), secondary electron detector, accelerating voltage 1–10 kV) and transmission electron microscopy (JEOL, JEM-1011, Akishima, Japan), and by X-ray spectral elemental microanalysis (INCA X-MAX 80 energy dispersive X-ray (EDX) spectrometer, Oxford Instruments (Oxford, UK), accelerating voltage 20 kV). X-ray diffraction was performed on powders and films using a D8 Advance (Bruker, Billerica, MA, USA, CuKα = 1.5418 Å, Ni filter, E = 40 keV, I = 40 mA; 2θ range: 5–45°; resolution: 0.02°; point accumulation time: 0.3 s).

A Renishaw (New Mills Wotton-under-Edge, Gloucestershire, UK, GL12 8JR) inVia Reflex Microscope system equipped with a Peltier-cooled CCD (532-nm Nd:YAG laser line was used) was used to record Raman spectra. The laser light was focused on the sample to ~2 μm through a 50× objective (power on the sample was <0.3 mW). A THMS600 stage (Linkam Scientific Instruments Ltd., Redhill, Unit 9, Perrywood Business Park, Honeycrock Lane, Salfords, Redhill, UK, Surrey RH1 5DZ) was used to record variable temperature Raman scattering. The *in-situ* film heating rate was 5 °C/min. The sample temperature was pre-calibrated using a high-precision Testo 868 thermal imaging camera. When recording Raman spectra, there is local heating of the imaging area, so the spectra were recorded in different areas of the film, but close to each other. All spectra were normalized with respect to the most intense spectrum.

The chemoresistive responses were performed at room temperature using the laboratory setup described in [41]. A gas-air atmosphere was created in a quartz cell (volume -7×10^{-5} m^3) using two Bronkhorst gas flow controllers with a maximum throughput of 100 and 200 mL/min. The electrical properties of the oxide films obtained were measured using a Fluke 8846A Digit Precision Multimeter with an upper detection limit of 1000 MΩ. The sensor temperature was monitored using a pre-calibrated platinum micro-heater. Prior to gas-sensitive measurements, the film was held in a baseline gas atmosphere until a stable signal was obtained.

Different relative humidities (RH) were generated using a special unit with a bubbler flask. The RH of the gas mixture was measured with a digital flow hygrometer "Excis" (EXIS, Russia, Moscow). The temperature value of the relative humidity was set and then measured at 20 °C.

All gas-sensing measurements were performed at room temperature (RT) and 0% RH. The response to H_2, CO, NH_3, benzene (C_6H_6), acetone (C_3H_6O), methane (CH_4) and ethanol (C_2H_5OH) were calculated using the following ratio:

$$S_1 = \frac{|R_{BL} - R_g|}{R_{BL}} \times 100\% \quad (1)$$

where R_{BL}—baseline resistance (synthetic air was used as the baseline gas), R_g—resistance at a given concentration of analyte gas.

The response to humidity was calculated using the following ratio:

$$S_2 = \frac{|R_{BL} - R_{RH}|}{R_{BL}} \times 100\% \quad (2)$$

where R_{BL}—resistance at 0% relative humidity, R_{RH}—at a given relative humidity.

3. Results and Discussion

3.1. The Phase Composition and Microstructure of the Obtained V_2CT_x MXene before Oxidation

Figure 1a shows the X-ray patterns of the V_2AlC MAX-phase powders that were used for the synthesis, as well as an X-ray pattern of the resulting V_2CT_x MXene powder. As can be seen, the set of V_2AlC MAX-phase reflexes correlates well with the data reported in the literature (V_2AlC, ICSD-606283, Space group *P6₃/mmc*). In addition to the characteristic intense reflex (002) at 2θ = 7.4° on the X-ray pattern of the obtained V_2CT_x MXene sample, there are reflexes of impurity phases: the V_2AlC MAX-phase and the cubic vanadium carbide phase VC (ICSD-159870, Space group *Fm-3m*), which should not affect the gas sensitive properties of MXene. The position of the observed reflex (002) for V_2CT_x MXene is in good agreement with other experimental data for this compound [42–44]. Figure 1b shows an X-ray pattern of the V_2CT_x MXene film before oxidation on an Al_2O_3 substrate. Because of the low thickness of the obtained film, only the characteristic set of α-Al_2O_3 substrate reflexes (PDF 00-005-0712) is clearly visible in the X-ray pattern shown. The inset on the left shows a region of the X-ray pattern in the 2θ = 4.5–12° interval with a long signal accumulation time at the point where a widened reflex (002) of the V_2CT_x MXene phase is observed. Its position is in good agreement with both the literature data and the data obtained for the powder of the corresponding composition in the present study (Figure 1a).

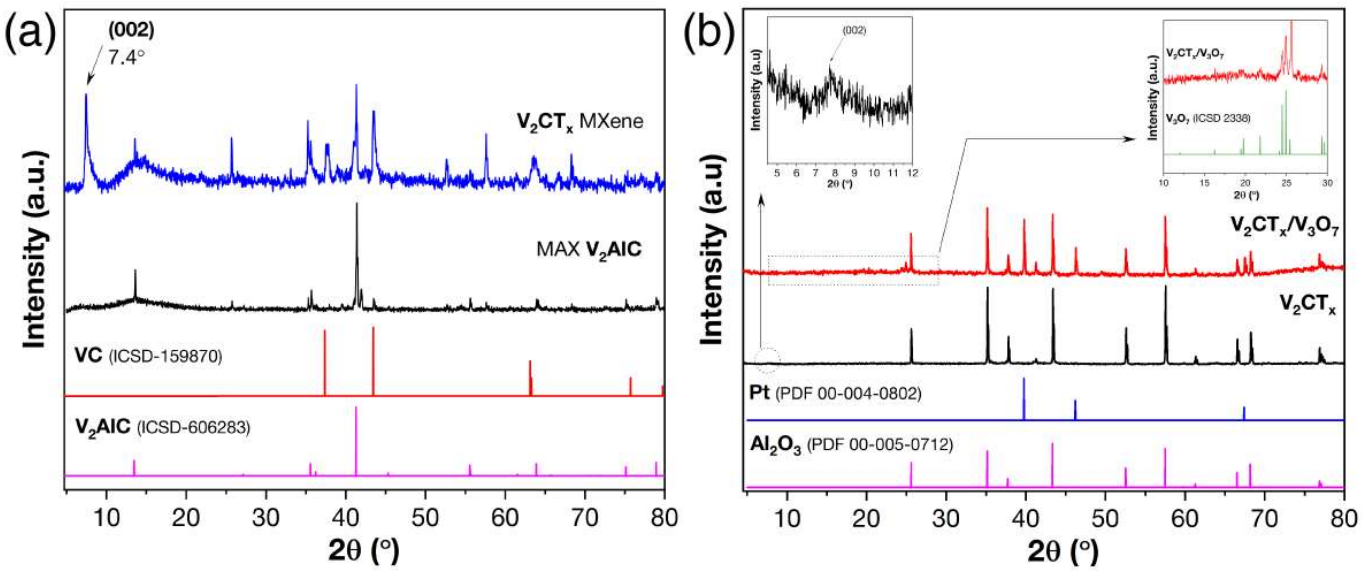

Figure 1. X-ray patterns of the V_2AlC MAX-phase and the obtained accordion-like V_2CT_x MXene powder (**a**), as well as V_2CT_x MXene films on Al_2O_3/Pt substrates before and after in situ oxidation with insets of characteristic bands for the corresponding V_2CT_x MXene (left) and V_3O_7 (right) phases (**b**).

Figure 2 shows SEM and TEM micrographs of the synthesized V_2CT_x MXene powder. The microstructure of V_2CT_x MXene has an accordion-like structure typical of this fabrication technique. The average interlayer distance was calculated from the Figure 2a micrograph, and was found to be 22 ± 5 nm. The value obtained is quite high, indicating a large specific surface area of the obtained multilayer V_2CT_x MXene, which is important for gas sensing. The TEM data (Figure 2c) confirm the formation of the multilayer harmonic, which is in good agreement with the SEM data. Figure 3a–c shows SEM micrographs of the V_2CT_x MXene film on an

Al_2O_3 substrate. As can be observed from the presented data, the microstructure of the films is in complete agreement with the microstructure of the powder: the accordion-like structure of the MXene is maintained, the interlayer spacing values are in the range of the calculated values for the powder. Using EDX analysis, it was found that besides C, V, forming elements V_2CT_x MXene and aluminum (typical for an impurity of the initial MAX-phase V_2AlC or aluminum fluorides), the MXene surface *T*-functional groups contain oxygen, fluorine and chlorine (Figure 4a). Their ratio n(F):n(Cl) = 19:1 is determined by peculiarities of the selective etching process by the chosen system (HF + HCl).

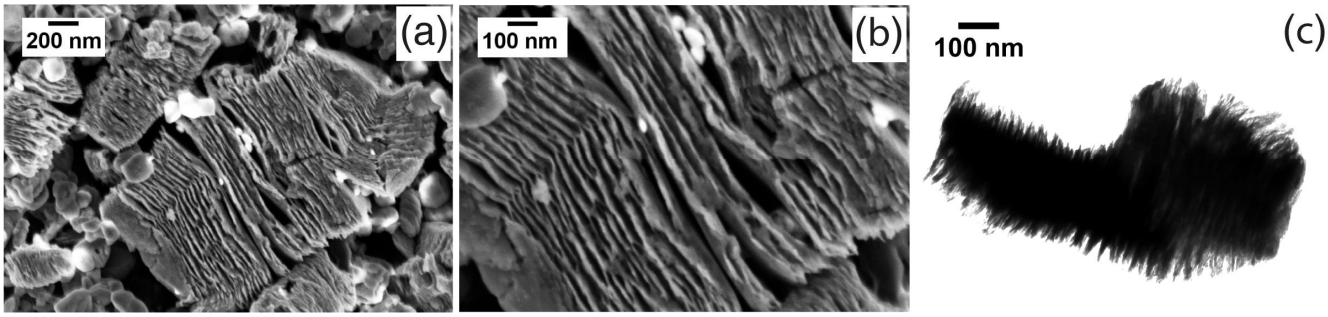

Figure 2. SEM (**a**,**b**) and TEM (**c**) microphotographs of V_2CT_x MXene powder.

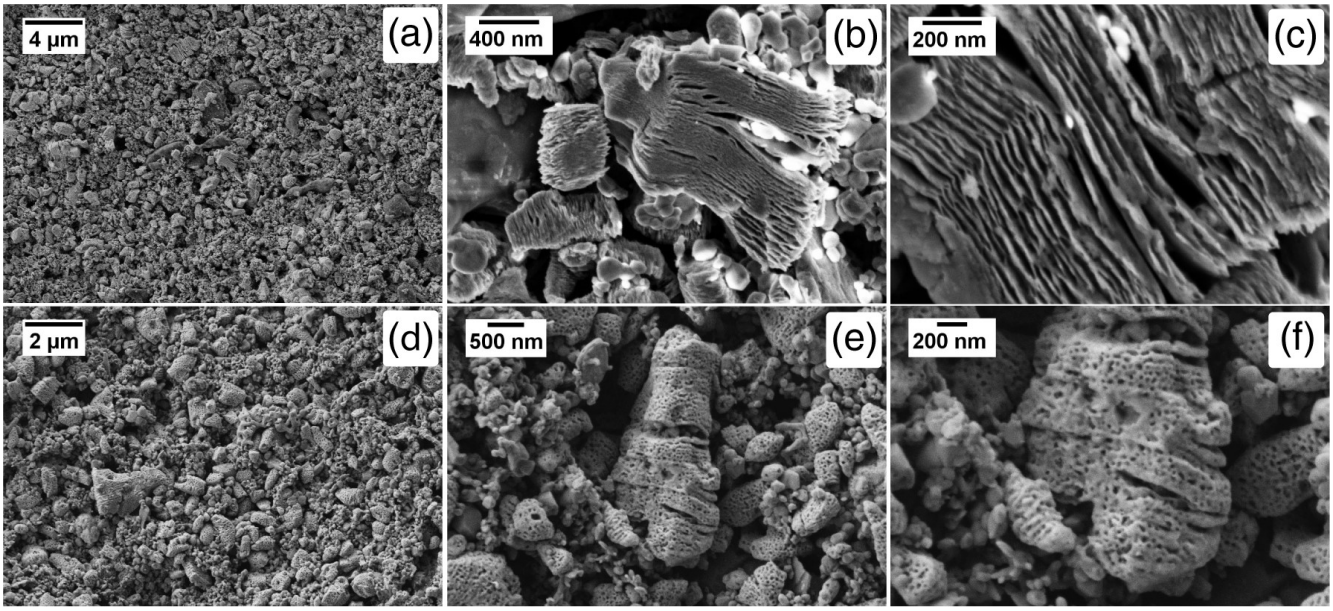

Figure 3. SEM micrographs of V_2CT_x MXene film on Al_2O_3/Pt substrates before (**a**–**c**) and after (**d**–**f**) oxidation.

3.2. Thermal Analysis of V_2CT_x Powder

The study of the thermal behavior of the obtained V_2CT_x multilayer powder sample during its heating in an air flow (Figure 4b) allows for a more correct planning of the experiment in the *in-situ* oxidation of the MXene receptor layer during heating during the recording of Raman spectra. Thus, in the initial stages of heating at temperatures <120–230 °C there is a mass loss of ~1.6–1.7%, probably due to the removal of adsorbed water molecules. On heating >240 °C there is a further decrease in mass, which may be due to the removal of MXene functional groups, primarily OH-groups. This process at temperatures above 240–260 °C is overlaid by exothermic processes of the beginning of MXene oxidation: with a maximum at 300 °C for more dispersed MXene aggregates (a stack diameter of 100–300 nm), surface areas of larger V_2CT_x aggregates (~500–1000 nm stack diameter) and

internal areas of large accordion-like aggregates, to which diffusion is difficult (with a maximum at 352 °C). In this case, the oxidation process becomes dominant at 350 °C, as the decrease in mass loss due to functional groups removal is replaced by a tendency to increase in mass. A low intensity exothermic effect in the interval 490–570 °C can be attributed to the oxidation of more oxidation-resistant phases VC and V_2AlC. Thus, the onset of the oxidation process of V_2CT_x MXene with simultaneous heating in air and recording of Raman spectra should be expected at temperatures ~240–250 °C.

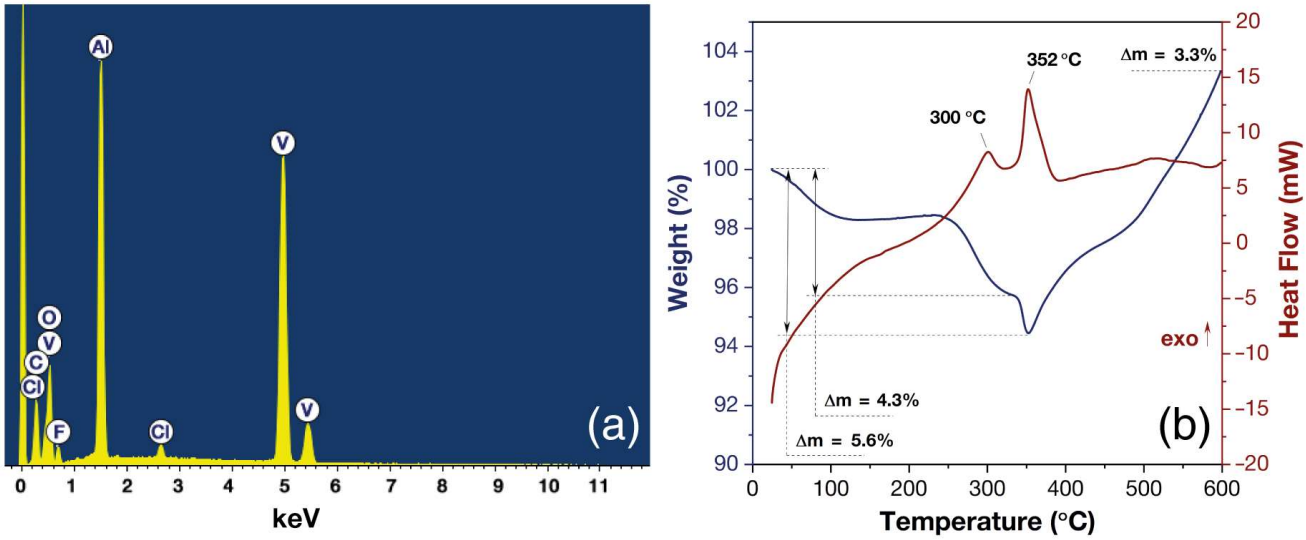

Figure 4. EDX spectrum of V_2CT_X film on Al_2O_3 substrate (**a**) and DSC (red) and TGA (blue) curves of the obtained V_2CT_x powder during heating in an air current (**b**).

3.3. In Situ Raman Spectroscopy during Heating of V_2CT_x MXene Film

The main purpose of using in situ Raman spectroscopy in the present study was to study the oxidation process of the V_2CT_x MXene film as well as the formation of the V_2CT_x/VO_x composite for further study of the gas-sensitive properties.

Figure 5 shows the *in-situ* Raman spectra of the V_2CT_x MXene film when heated in the temperature range RT–250 °C. At room temperature, four MXene characteristic modes ω_1–ω_4 are observed at 269, 431, 689 and 912 cm^{-1}, respectively. These modes can be related to the individual V_2CT_x MXene [36,45–47]. In addition, D-(ω_D) and G-modes (ω_G) are present in the spectra at 1354 and 1582 cm^{-1}, which are common to many carbon systems with sp^2-hybridization of carbon atoms [48]. The presence of D- and G-modes is characteristic of the entire MXene family; it illustrates the formation of layered carbon in their composition or the formation of a graphene-like carbon impurity during excessive etching of the MAX-phase. The described set of characteristic modes ω_1–ω_4 and ω_D, ω_G is maintained up to 200 °C. It is worth noting that all modes except for the D- and G-bands are of low-intensity, which is a consequence of two factors: the nature of the MXenes themselves, which are not characterized by intense Raman bands, and the conditions of the Raman experiment, since the study was performed at low laser power to avoid local overheating of the coating by the laser itself and MXene oxidation. In addition, as we have recently shown for Ti_2CT_x [40], the MXene modes on the Al_2O_3 substrate are much weaker than on the platinum substrate.

The changes in the Raman spectra of the V_2CT_x MXene film start to appear at 250 °C. In addition, new modes are added to the V_2CT_x MXene ω_1–ω_4 bands: intense ω_5 at 144 cm^{-1} as well as ω_6–ω_{11} at 280, 306, 409, 525, 700 and 995 cm^{-1}, respectively. The Raman bands described are characteristic of α-V_2O_5 (orthorhombic crystal lattice, Space group *Pmmn*) [49]: B_{2g}, B_{1g}, A_{1g}, A_{1g}, A_{1g} and (A_{1g} and B_{2g}) modes, respectively [50]. It should be noted that the D- and G-modes are maintained at the heating temperature of 250 °C, which also confirms the fact that the MXene oxidation did not proceed completely

and the V_2CT_x/V_2O_5 composite was formed at these temperature conditions. Thus, the temperature of 250 °C was chosen as optimal for in situ heating of the V_2CT_x MXene film using Raman spectroscopy.

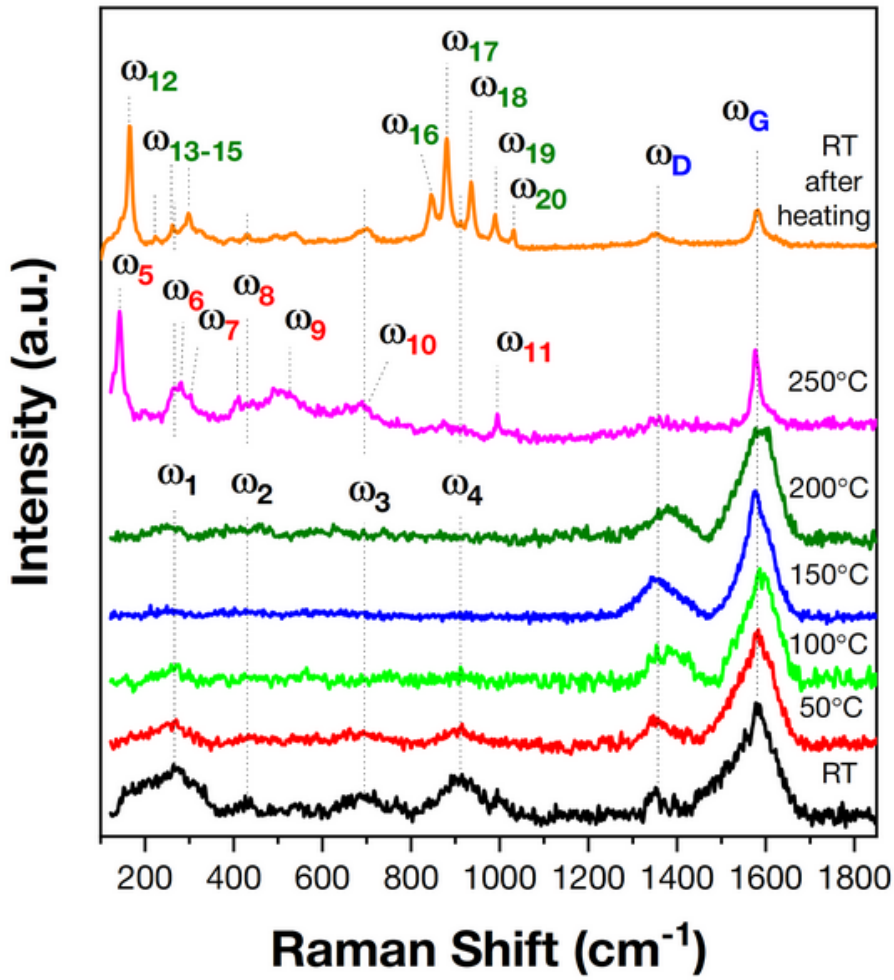

Figure 5. In situ Raman spectra during heating of V_2CT_x MXene film in air in the temperature range RT–250 °C.

After cooling the sample to room temperature, Raman spectra were also recorded for the obtained oxidized V_2CT_x MXene film. It was found that the spectrum obtained is significantly different from that recorded for the sample heated to 250 °C (Figure 5). The spectrum contains a completely different set of Raman modes: ω_{12}–ω_{20} at 168 (intense), 224, 261, 298, 845, 880 (intense), 936, 990 and 1031 cm^{-1}, respectively, which correspond with high accuracy to the characteristic peaks for another vanadium oxide, V_3O_7 (monoclinic crystal lattice, Space group *C2/c*) [50]. It is to be noted that the ω_1–ω_3 and ω_D–ω_D modes characteristic of V_2CT_x MXene are maintained in the spectrum, indicating that the V_2CT_x/V_3O_7 composite has formed during cooling. Thus, after cooling from 250 °C to room temperature, the obtained film undergoes structural changes: the vanadium (V) oxide α-V_2O_5 formed during MXene oxidation is transformed into the mixed oxide V_3O_7 containing vanadium atoms in the +IV and +V oxidation states. It is worth noting that the formation of V_3O_7 is not a common case for vanadium oxides, which are characterized by individual V_2O_5 and VO_2 oxides, as well as composites containing their individual phases [49,51].

3.4. The Phase Composition and Microstructure of the Obtained V_2CT_x MXene after Oxidation

Figure 1b shows an X-ray pattern of the V_2CT_x/V_3O_7 film on an Al_2O_3/Pt substrate after heating to 250 °C using in situ Raman spectroscopy. It shows intense reflexes related to the substrate materials α-Al_2O_3 and Pt (PDF 00-005-0712 and 00-004-0802, respectively), as well as low-intensity reflexes of the V_3O_7 phase. The resulting set of V_3O_7 reflexes correlates well with the available data in the database (ICSD 2338), which is particularly evident in the corresponding inset in Figure 1b, right. The XRD data obtained are in full agreement with the Raman data and confirm the V_3O_7 content in the films obtained after heating to 250 °C in air.

Figure 3d–f shows SEM microphotographs of V_2CT_x/V_3O_7 films after heating to 250 °C using in situ Raman spectroscopy; it is shown that the microstructure of the films undergoes significant changes. The microphotographs show a shape similar to the initial multilayer harmonic, which is characteristic of MXene, but this is no longer observed after oxidation. The formed structures become more closed and porous with a pore size of ~25–40 nm, which is close to the value of the interlayer distances that were calculated for the individual multilayer aggregates of V_2CT_x MXene.

3.5. Gas-Sensing Chemoresistive Properties

In the first step, chemoresistive responses were determined for the obtained V_2CT_x and V_2CT_x/V_3O_7 films when detecting 100 ppm CO, NH_3, NO_2, benzene (C_6H_6), acetone (C_3H_6O), ethanol (C_2H_5OH), and 1000 ppm methane (CH_4) and H_2 at room temperature and 0% RH. Experimental responses (S1) for these gases are shown in Figure 6a,b. Selectivity diagrams (Figure 6c,d) were constructed from the series of responses obtained. The obtained responses for V_2CT_x do not show high numerical values; nevertheless, due to the high SNR value (which is typical for the whole MXene family) it was possible to efficiently detect different gases. For the original V_2CT_x MXene film, the highest response (1.35%) was observed in the detection of NH_3. Notable responses were also recorded for NO_2 (0.96%) and CO (0.94%), while the response for all other analyzed gases did not exceed 0.55%. For the oxidized V_2CT_x/V_3O_7 MXene, a significant increase in the response value for all analyzed gases was observed: the response for NH_3 increased more than 9 times to 12.7%, and for NO_2 more than 15 times to 14.9%. The response to all other analyzed gases did not exceed 10.3%. The numerical values of the responses to all the studied gases of the MXene film before and after oxidation are shown in Figure 6c,d.

For ammonia, for which high responses were observed during detection, the sensitivity to different concentrations was studied. Figure 7a,b shows the responses to 4–100 ppm NH_3 at RT of the MXene film before and after oxidation. As can be seen, there is a consistent increase in the response (S1) with increasing NH_3 concentrations from 4 to 100 ppm in both cases: from 0.18 to 1.35%, and from 2.7 to 12.7% for V_2CT_x and V_2CT_x/V_3O_7, respectively, with a small baseline drift (which can be explained by the high interaction energy of the ammonia molecule with the receptor material). Thus, both V_2CT_x and V_2CT_x/V_3O_7 films demonstrate the ability to precisely detect different analyte content in the gas atmosphere at room temperature.

Figure 7c,d shows the response of the obtained V_2CT_x and V_2CT_x/V_3O_7 films when the relative humidity RH is changed from 0 to 95%. For the original V_2CT_x film, the response (S2) is 10% when the RH is changed to 95%, which is quite high compared to the response for the other gases for which the response does not exceed 1.35%. The oxidized V_2CT_x/V_3O_7 film also shows a significant increase in sensitivity to RH: the response at 70% RH is 85.6%. At the same time, it should be noted that in the range RH = 50–95% the response to humidity changes much less significantly than at humidity <50%. In general, the high sensitivity of MXenes to humidity is typical and well-described in the literature, but we have not found any reports in the available sources of an increase in their sensitivity to humidity during the formation of the V_2CT_x/V_3O_7 composite.

Figure 8 shows a column diagram of the selectivity, taking into account the sign of the response. Positive values correspond to an increase in electrical resistance (*p*-response), and

negative values correspond to a decrease (*n*-response). As can be seen from the presented data, for the original V_2CT_x MXene film in the detection of all gases (including an increase in RH) there is a *p*-response, which is typical for MXene, except for NO_2, for which an *n*-response is recorded. However, for the oxidized V_2CT_x/V_3O_7 film, significant changes are observed: for all gases, except NH_3 and NO_2, the response is reversed from *p*- to *n*-response. When NH_3 is detected, the *p*-type response is retained, and when NO_2 is detected, the *n*-type response is retained. The observed processes with the change of direction of resistance change are a consequence of the change of mechanisms of gas detection.

In the detection of various gases, the *p*-response (with an increase of resistance at the analyte injection) is quite typical for various individual MXenes, including V_2CT_x [33]. The resistance increase observed in this case can be explained by the so-called "swelling mechanism", according to which gases can intercalate into the MXenes' interlayer space, which causes an additional increase in the interlayer distance, complicating the charge transfer outside the MXenes plane [33]. In addition, it is believed that the sorption of any gases due to the charge transfer between them and the MXenes metal atoms interferes with the transport of charge carriers and reduces their quantity.

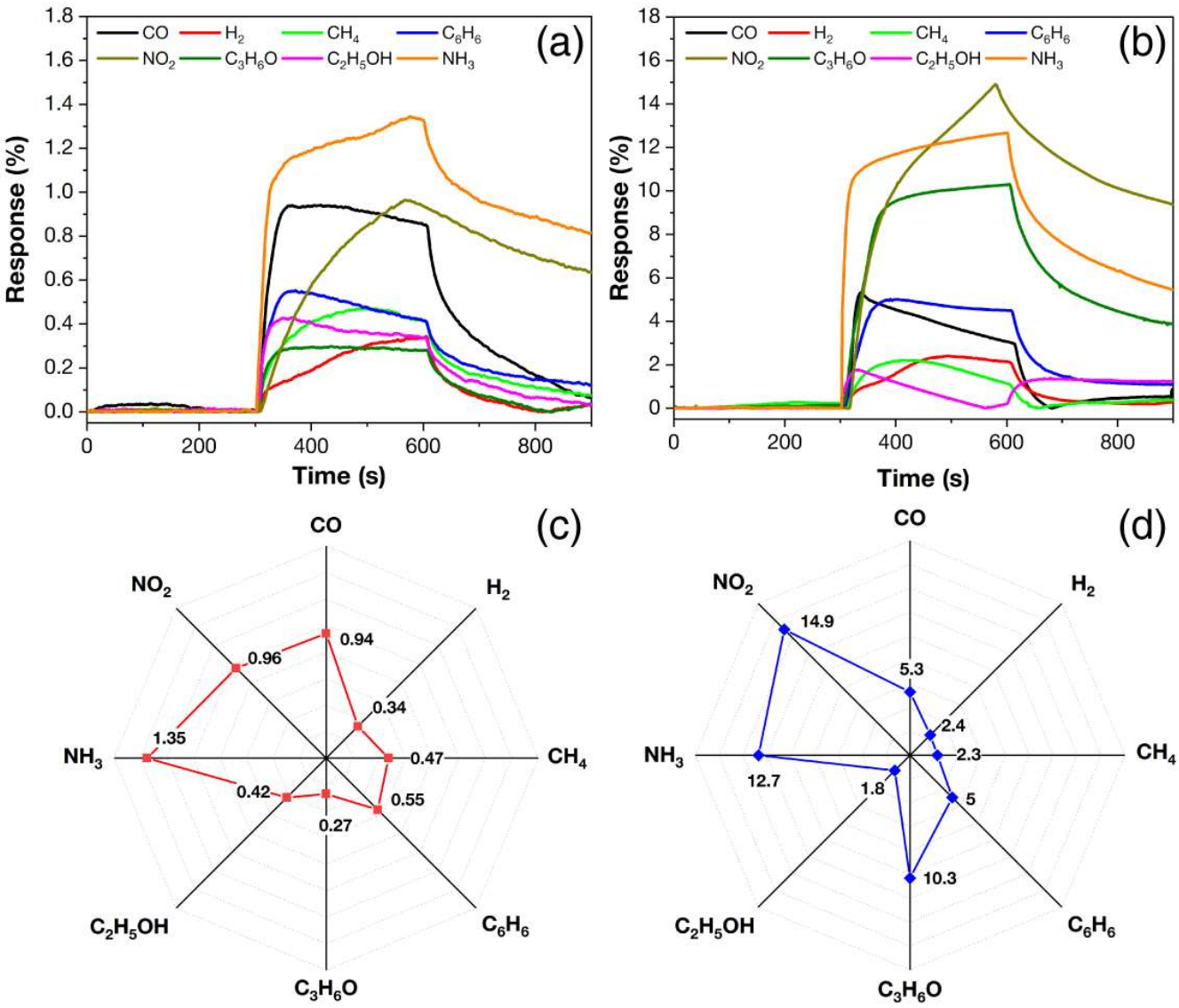

Figure 6. Responses (%) to various gases (100 ppm CO, NH_3, NO_2, C_6H_6, C_3H_6O, C_2H_5OH and 1000 ppm CH_4, H_2) and V_2CT_x MXene film selectivity diagrams before (**a**,**c**) and after oxidation (**b**,**d**); all data obtained at RT and 0%RH.

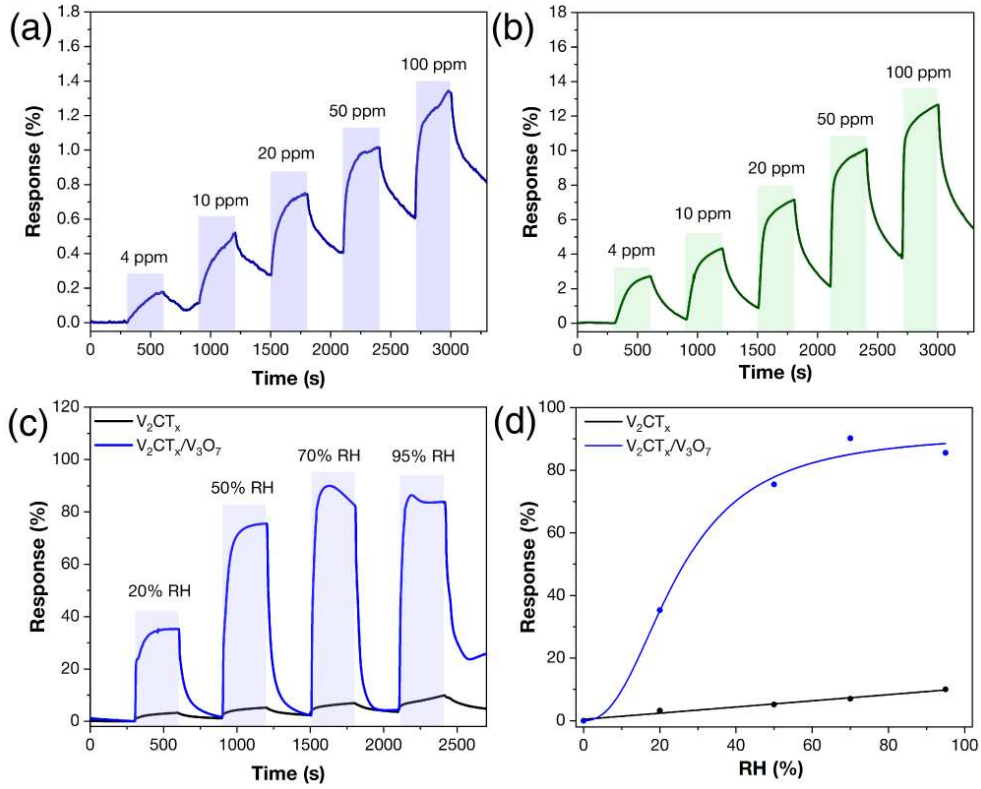

Figure 7. Responses (%) to 4–100 ppm NH_3 of V_2CT_x MXene film before (**a**) and after oxidation (**b**) at RT and 0%RH; responses to 20–95%RH (**c**,**d**) at RT.

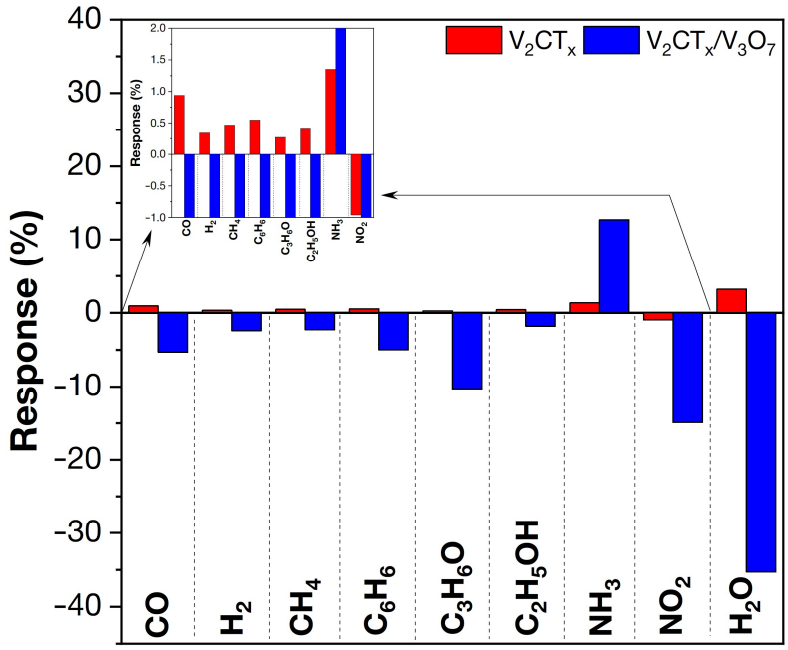

Figure 8. The selectivity diagram of V_2CT_x MXene film and V_2CT_x/V_3O_7 nanocomposite summarizing the response data (taking into account the sign of response, i.e., the direction of resistance change. The "+" sign corresponds to an increase in electrical resistance, and the "−" sign to a decrease) for different gases (100 ppm CO, NH_3, NO_2, C_6H_6, C_3H_6O, C_2H_5OH, 1000 ppm CH_4, H_2 and 20%RH), with the inset with a large increase in response value for some gases.

As in the case described in the present study, the investigation by Yajie Zhang et al. [32] also recorded an *n*-response in the detection of NO_2, which the authors associated with possible reactions between the NO_2 molecule and the functional groups -O and -OH on the surface of the V_2CT_x MXene. As a result, NO_2^--groups may be formed on the MXene surface, which leads to a decrease in electrical resistance. This mechanism is supported by the fact that, according to EDX analysis, the V_2CT_x powder obtained contains a large number of oxygen-containing fragments (O, OH and probably H_2O in the interlayer space) in addition to F- and Cl-groups, which may also be involved in the gas-sensing mechanism and influence the response characteristics [31]. There are a few studies in the literature on the use of an individual V_2CT_x as a sensor material; nevertheless, the available data are in good agreement with the data obtained in the present study [31–34].

Vanadium dioxide (VO_2) and vanadium pentaoxide (V_2O_5) are known to be *n*-type semiconductors [52,53]. The vanadium oxide (V_3O_7) formed in this case is intermediate between VO_2 and V_2O_5 and is also an *n*-type semiconductor. The *n*-type response obtained when the V_2CT_x/V_3O_7 film detected all the gases studied except NH_3 can be explained by the classical detection mechanism for MOS-sensors through the ion adsorbed oxygen on the surface of the V_3O_7 semiconductor nanoparticles [54–56]. CO, C_6H_6, C_3H_6O, C_2H_5OH, CH_4 and H_2 are reducing gases, so when they react with ionized oxygen (O_y^{x-}), they should oxidize to form CO_2 and H_2O, which can lead to the release of additional electrons while the electrical resistance decreases, corresponding to an *n*-response [57–60]. The obtained data on the sensing properties agree well with those reported in the literature for V_2O_5 [30] at elevated sensing temperatures. When NH_3 and NO_2 were detected by the V_2CT_x/V_3O_7 nanocomposite film, *p*- and *n*-responses, respectively, were observed (i.e., the detection character of V_2CT_x MXene was maintained), which is not typical for *n*-type semiconductors. In this regard, it can be assumed that the detection of these gases is mainly due to the characteristic of the MXene mechanism.

The increase in response values for the V_2CT_x/V_3O_7 nanocomposite can be associated with the formation of metal defects in the MXene layers during oxidation and the increase in specific surface area that improved adsorption of gases, as well as with the formation of heterojunctions. This leads to an effective separation of charge carriers at the interface and increases the sensitivity to adsorption of electron-donor and -acceptor gases.

It is to be noted that the oxidation of the V_2CT_x film also changes the direction of the humidity-sensing response from the *n*- to the *p*-type. For the individual V_2CT_x film, the *p*-type response with increasing humidity is also traditionally explained by the swelling mechanism resulting from the adsorption of molecules between the MXene layers. On the other hand, the *n*-type response of the V_2CT_x/V_3O_7 composite film can be explained by the mechanisms of the interaction of water molecules with MOS-materials [54], according to which hydroxylgroups are formed on the surface of the metal oxide semiconductor. As a result, electrons are emitted and a decrease in electrical resistance is observed, which corresponds to the *n*-response [27].

Separately, it should be noted that there are no data in the literature on the use of V_3O_7 as a gas-sensitive chemoresistive material. This fact can be explained by the metastability of this oxide, and the operation of MOS-gas sensors usually occurs at elevated temperatures. The data obtained in this study are probably the first experimental confirmation of the high gas sensitivity of this oxide.

4. Conclusions

In summary, the present study is the first to investigate the effect on the gas-sensitive properties of accordion-like V_2CT_x MXene synthesized by selective etching of V_2AlC MAX-phase by HF-HCl acid mixture, and doping with nanosized V_3O_7 as a result of MXene oxidation controlled in situ by Raman spectroscopy.

The elemental and phase composition, the microstructure of the synthesized V_2CT_x MXene, the coatings based on it, and the V_2CT_x/V_3O_7 nanocomposite obtained at a minimum oxidation temperature of 250 °C were studied by using a variety of physical and chemical analytical methods.

It was found that the obtained V_2CT_x and V_2CT_x/V_3O_7 films are sensitive at room temperature and zero humidity to a wide range of investigated gases (H_2, CO, NH_3, C_6H_6, C_3H_6O, CH_4, C_2H_5OH and NO_2), but the highest responses were observed for ammonia and nitrogen dioxide. At the same time, the partial oxidation of V_2CT_x leads not only to an increase in the response of the V_2CT_x/V_3O_7 material, but also to some change in selectivity. Thus, if for the original V_2CT_x multilayer MXene the responses at 100 ppm (RT, RH = 0%) decreased in the series NH_3 (1.35%) > NO_2 (0.96%) > CO (0.94%), then for the V_2CT_x/V_3O_7 composite the series of highest responses changes: NO_2 (14.9%) > NH_3 (12.7%) > acetone (10.3). Despite the close response values for NO_2 and NH_3, this does not negatively affect the selectivity due to the different nature of the resistance change when these gases are injected.

It is shown that the oxidation of the V_2CT_x film and the formation of the V_2CT_x/V_3O_7 nanocomposite also leads to a significant increase in the humidity response value (RH = 0–95%) and a change in its character from *n*- to *p*-type. At the same time, for V_2CT_x/V_3O_7 there is a saturation of the response value after reaching the relative humidity of 50%, in contrast to the initial V_2CT_x MXene.

Author Contributions: Conceptualization, A.S.M., N.P.S. and E.P.S.; methodology, N.T.K.; validation, E.P.S. and N.T.K.; investigation, A.S.M., I.A.N., A.A.A., T.L.S. and N.P.S.; resources, N.T.K.; writing—original draft preparation, A.S.M., I.A.N., A.A.A. and T.L.S.; writing—review and editing, I.A.N. and E.P.S.; supervision, N.T.K.; project administration, N.P.S.; funding acquisition, N.P.S. All authors have read and agreed to the published version of the manuscript.

Funding: This work was supported by the Russian Science Foundation, project No. 21-73-10251, https://rscf.ru/en/project/21-73-10251/ (accessed on 30 January 2023).

Institutional Review Board Statement: Not applicable.

Informed Consent Statement: Not applicable.

Data Availability Statement: Not applicable.

Conflicts of Interest: The authors declare no conflict of interest.

References

1. Naguib, M.; Mashtalir, O.; Carle, J.; Presser, V.; Lu, J.; Hultman, L.; Gogotsi, Y.; Barsoum, M.W. Two-Dimensional Transition Metal Carbides. *ACS Nano* **2012**, *6*, 1322–1331. [CrossRef] [PubMed]
2. Naguib, M.; Mochalin, V.N.; Barsoum, M.W.; Gogotsi, Y. 25th Anniversary Article: MXenes: A New Family of Two-Dimensional Materials. *Adv. Mater.* **2014**, *26*, 992–1005. [CrossRef] [PubMed]
3. Li, X.; An, Z.; Lu, Y.; Shan, J.; Xing, H.; Liu, G.; Shi, Z.; He, Y.; Chen, Q.; Han, R.P.S.; et al. Room Temperature VOCs Sensing with Termination-Modified $Ti_3C_2T_x$ MXene for Wearable Exhaled Breath Monitoring. *Adv. Mater. Technol.* **2022**, *7*, 2100872. [CrossRef]
4. Wang, J.; Xu, R.; Xia, Y.; Komarneni, S. Ti_2CT_x MXene: A Novel p-Type Sensing Material for Visible Light-Enhanced Room Temperature Methane Detection. *Ceram. Int.* **2021**, *47*, 34437–34442. [CrossRef]
5. Lee, J.; Kang, Y.C.; Koo, C.M.; Kim, S.J. $Ti_3C_2T_x$ MXene Nanolaminates with Ionic Additives for Enhanced Gas-Sensing Performance. *ACS Appl. Nano Mater.* **2022**, *5*, 11997–12005. [CrossRef]
6. Majhi, S.M.; Ali, A.; Greish, Y.E.; El-Maghraby, H.F.; Qamhieh, N.N.; Hajamohideen, A.R.; Mahmoud, S.T. Accordion-like-Ti_3C_2 MXene-Based Gas Sensors with Sub-ppm Level Detection of Acetone at Room Temperature. *ACS Appl. Electron. Mater.* **2022**, *4*, 4094–4103. [CrossRef]
7. Ho, D.H.; Choi, Y.Y.; Jo, S.B.; Myoung, J.M.; Cho, J.H. Sensing with MXenes: Progress and Prospects. *Adv. Mater.* **2021**, *33*, 2005846. [CrossRef]
8. Alwarappan, S.; Nesakumar, N.; Sun, D.; Hu, T.Y.; Li, C.Z. 2D Metal Carbides and Nitrides (MXenes) for Sensors and Biosensors. *Biosens. Bioelectron.* **2022**, *205*, 113943. [CrossRef]
9. Ganesh, P.S.; Kim, S.Y. Electrochemical Sensing Interfaces Based on Novel 2D-MXenes for Monitoring Environmental Hazardous Toxic Compounds: A Concise Review. *J. Ind. Eng. Chem.* **2022**, *109*, 52–67. [CrossRef]

10. SiSivasankarapillai, V.S.; Sharma, T.S.K.; Wabaidur, K.Y.H.S.M.; Angaiah, S.; Dhanusuraman, R. MXene Based Sensing Materials: Current Status and Future Perspectives. *ES Energy Environ.* **2022**, *5*, 4–14. [CrossRef]
11. Zhao, Q.; Zhou, W.; Zhang, M.; Wang, Y.; Duan, Z.; Tan, C.; Liu, B.; Ouyang, F.; Yuan, Z.; Tai, H.; et al. Edge-Enriched $Mo_2TiC_2T_x/MoS_2$ Heterostructure with Coupling Interface for Selective NO_2 Monitoring. *Adv. Funct. Mater.* **2022**, *32*, 2203528. [CrossRef]
12. Nahirniak, S.; Saruhan, B. MXene Heterostructures as Perspective Materials for Gas Sensing Applications. *Sensors* **2022**, *22*, 972. [CrossRef] [PubMed]
13. Devaraj, M.; Rajendran, S.; Hoang, T.K.A.; Soto-Moscoso, M. A Review on MXene and Its Nanocomposites for the Detection of Toxic Inorganic Gases. *Chemosphere* **2022**, *302*, 134933. [CrossRef]
14. Sett, A.; Rana, T.; Rajaji, U.; Sha, R.; Liu, T.Y.; Bhattacharyya, T.K. Emergence of Two-Dimensional Nanomaterials-Based Breath Sensors for Non-Invasive Detection of Diseases. *Sens. Actuators A Phys.* **2022**, *338*, 113507. [CrossRef]
15. Wang, Z.; Yu, K.; Feng, Y.; Qi, R.; Ren, J.; Zhu, Z. VO_2(p)-V_2C(MXene) Grid Structure as a Lithium Polysulfide Catalytic Host for High-Performance Li-S Battery. *ACS Appl. Mater. Interfaces* **2019**, *11*, 44282–44292. [CrossRef]
16. Shan, Q.; Mu, X.; Alhabeb, M.; Shuck, C.E.; Pang, D.; Zhao, X.; Chu, X.F.; Wei, Y.; Du, F.; Chen, G.; et al. Two-Dimensional Vanadium Carbide (V_2C) MXene as Electrode for Supercapacitors with Aqueous Electrolytes. *Electrochem. Commun.* **2018**, *96*, 103–107. [CrossRef]
17. Zhou, J.; Gao, S.; Guo, Z.; Sun, Z. Ti-Enhanced Exfoliation of V_2AlC into V_2C MXene for Lithium-Ion Battery Anodes. *Ceram. Int.* **2017**, *43*, 11450–11454. [CrossRef]
18. Tan, H.; Wang, C.; Duan, H.; Tian, J.; Ji, Q.; Lu, Y.; Hu, F.; Hu, W.; Li, G.; Li, N.; et al. Intrinsic Room-Temperature Ferromagnetism in V_2C MXene Nanosheets. *ACS Appl. Mater. Interfaces* **2021**, *13*, 33363–33370. [CrossRef]
19. Zada, S.; Lu, H.; Yang, F.; Zhang, Y.; Cheng, Y.; Tang, S.; Wei, W.; Qiao, Y.; Fu, P.; Dong, H.; et al. V_2C Nanosheets as Dual-Functional Antibacterial Agents. *ACS Appl. Bio Mater.* **2021**, *4*, 4215–4223. [CrossRef]
20. He, N.; Zhang, Q.; Tao, L.; Chen, X.; Qin, Q.; Liu, X.; Lian, X.; Wan, X.; Hu, E.; Xu, J.; et al. VC-Based Memristor for Applications of Low Power Electronic Synapse. *IEEE Electron. Device Lett.* **2021**, *42*, 319–322. [CrossRef]
21. Liu, H.; Lu, C.; Wang, X.; Xu, L.; Huang, X.; Wang, X.; Ning, H.; Lan, Z.; Guo, J. Combinations of V2C and Ti_3C_2 MXenes for Boosting the Hydrogen Storage Performances of MgH_2. *ACS Appl. Mater. Interfaces* **2021**, *13*, 13235–13247. [CrossRef] [PubMed]
22. Chen, Y.; Yao, H.; Kong, F.; Tian, H.; Meng, G.; Wang, S.; Mao, X.; Cui, X.; Hou, X.; Shi, J. V_2C MXene Synergistically Coupling FeNi LDH Nanosheets for Boosting Oxygen Evolution Reaction. *Appl. Catal. B Environ.* **2021**, *297*, 120474. [CrossRef]
23. Junkaew, A.; Arróyave, R. Enhancement of the Selectivity of MXenes (M_2C, M = Ti, V, Nb, Mo) via Oxygen-Functionalization: Promising Materials for Gas-Sensing and -Separation. *Phys. Chem. Chem. Phys.* **2018**, *20*, 6073–6082. [CrossRef] [PubMed]
24. Choi, S.J.; Kim, I.D. *Recent Developments in 2D Nanomaterials for Chemiresistive-Type Gas Sensors*; The Korean Institute of Metals and Materials: Seoul, Republic of Korea, 2018; Volume 14, ISBN 0123456789.
25. Lee, E.; Kim, D.-J. Review—Recent Exploration of Two-Dimensional MXenes for Gas Sensing: From a Theoretical to an Experimental View. *J. Electrochem. Soc.* **2020**, *167*, 037515. [CrossRef]
26. Kim, S.J.; Koh, H.J.; Ren, C.E.; Kwon, O.; Maleski, K.; Cho, S.Y.; Anasori, B.; Kim, C.K.; Choi, Y.K.; Kim, J.; et al. Metallic $Ti_3C_2T_x$ MXene Gas Sensors with Ultrahigh Signal-to-Noise Ratio. *ACS Nano* **2018**, *12*, 986–993. [CrossRef]
27. Mokrushin, A.S.; Nagornov, I.A.; Simonenko, T.L.; Simonenko, N.P.; Gorobtsov, P.Y.; Arkhipushkin, I.A.; Simonenko, E.P.; Sevastyanov, V.G.; Kuznetsov, N.T. Gas-Sensitive Nanostructured ZnO Films Praseodymium and Europium Doped: Electrical Conductivity, Selectivity, Influence of UV Irradiation and Humidity. *Appl. Surf. Sci.* **2022**, *589*, 152974. [CrossRef]
28. Nagornov, I.A.; Mokrushin, A.S.; Simonenko, E.P.; Simonenko, N.P.; Sevastyanov, V.G.; Kuznetsov, N.T. Liquid-Phase Growth of Nanocrystalline ZnO Thin Films and Their Gas-Sensitive Properties. *Russ. J. Inorg. Chem.* **2022**, *67*, 539–546. [CrossRef]
29. Mokrushin, A.S.; Simonenko, T.L.; Simonenko, N.P.; Yu, P.; Bocharova, V.A.; Kozodaev, M.G.; Markeev, A.M.; Lizunova, A.A.; Volkov, I.A.; Simonenko, E.P.; et al. Microextrusion Printing of Gas-Sensitive Planar Anisotropic NiO Nanostructures and Their Surface Modification in an H2S Atmosphere. *Appl. Surf. Sci.* **2022**, *578*, 151984. [CrossRef]
30. Gorobtsov, P.Y.; Mokrushin, A.S.; Simonenko, T.L.; Simonenko, N.P.; Simonenko, E.P.; Kuznetsov, N.T. Microextrusion Printing of Hierarchically Structured Thick V_2O_5 Film with Independent from Humidity Sensing Response to Benzene. *Materials* **2022**, *15*, 7837. [CrossRef]
31. Wu, M.; An, Y.; Yang, R.; Tao, Z.; Xia, Q.; Hu, Q.; Li, M.; Chen, K.; Zhang, Z.; Huang, Q.; et al. V_2CT_x and $Ti_3C_2T_x$ MXenes Nanosheets for Gas Sensing. *ACS Appl. Nano Mater.* **2021**, *4*, 6257–6268. [CrossRef]
32. Zhang, Y.; Jiang, Y.; Duan, Z.; Huang, Q.; Wu, Y.; Liu, B.; Zhao, Q.; Wang, S.; Yuan, Z.; Tai, H. Highly Sensitive and Selective NO_2 Sensor of Alkalized V_2CT_x MXene Driven by Interlayer Swelling. *Sens. Actuators B Chem.* **2021**, *344*, 130150. [CrossRef]
33. Lee, E.; Vahidmohammadi, A.; Yoon, Y.S.; Beidaghi, M.; Kim, D.J. Two-Dimensional Vanadium Carbide MXene for Gas Sensors with Ultrahigh Sensitivity Toward Nonpolar Gases. *ACS Sens.* **2019**, *4*, 1603–1611. [CrossRef] [PubMed]
34. Wang, X.; Zhang, D.; Zhang, H.; Gong, L.; Yang, Y.; Zhao, W.; Yu, S.; Yin, Y.; Sun, D. In Situ Polymerized Polyaniline/MXene (V_2C) as Building Blocks of Supercapacitor and Ammonia Sensor Self-Powered by Electromagnetic-Triboelectric Hybrid Generator. *Nano Energy* **2021**, *88*, 106242. [CrossRef]

35. Wu, M.; Wang, B.; Hu, Q.; Wang, L.; Zhou, A. The Synthesis Process and Thermal Stability of V_2C MXene. *Materials* **2018**, *11*, 2112. [CrossRef]
36. Thakur, R.; Vahidmohammadi, A.; Moncada, J.; Adams, W.R.; Chi, M.; Tatarchuk, B.; Beidaghi, M.; Carrero, C.A. Insights into the Thermal and Chemical Stability of Multilayered V_2CT:X MXene. *Nanoscale* **2019**, *11*, 10716–10726. [CrossRef] [PubMed]
37. Simonenko, E.P.; Simonenko, N.P.; Nagornov, I.A.; Simonenko, T.L.; Mokrushin, A.S.; Sevastyanov, V.G.; Kuznetsov, N.T. Synthesis of MAX Phases in the Ti_2AlC–V_2AlC System as Precursors of Heterometallic MXenes $Ti_{2-X}V_xC$. *Russ. J. Inorg. Chem.* **2022**, *67*, 705–714. [CrossRef]
38. Simonenko, E.P.; Simonenko, N.P.; Nagornov, I.A.; Simonenko, T.L.; Gorobtsov, P.Y.; Mokrushin, A.S.; Kuznetsov, N.T. Synthesis and Chemoresistive Properties of Single-Layer MXene Ti_2CT_x. *Russ. J. Inorg. Chem.* **2022**, *67*, 1838–1847. [CrossRef]
39. Mokrushin, A.S.; Nagornov, I.A.; Gorobtsov, P.Y.; Averin, A.A.; Simonenko, T.L.; Simonenko, N.P.; Simonenko, E.P.; Kuznetsov, N.T. Effect of Ti_2CT_x MXene Oxidation on Its Gas-Sensitive Properties. *Chemosensors* **2023**, *11*, 13. [CrossRef]
40. Simonenko, N.P.; Glukhova, O.E.; Plugin, I.A.; Kolosov, D.A.; Nagornov, I.A.; Simonenko, T.L.; Varezhnikov, A.S.; Simonenko, E.P.; Sysoev, V.V.; Kuznetsov, N.T. The $Ti_{0.2}V_{1.8}C$ MXene Ink-Prepared Chemiresistor: From Theory to Tests with Humidity versus VOCs. *Chemosensors* **2023**, *11*, 7. [CrossRef]
41. Mokrushin, A.S.; Nagornov, I.A.; Simonenko, T.L.; Simonenko, N.P.; Yu, P.; Khamova, T.V.; Kopitsa, G.P.; Evzrezov, A.N.; Simonenko, E.P.; Sevastyanov, V.G.; et al. Chemoresistive Gas-Sensitive ZnO/Pt Nanocomposites Films Applied by Microplotter Printing with Increased Sensitivity to Benzene and Hydrogen. *Mater. Sci. Eng. B* **2021**, *271*, 115233. [CrossRef]
42. Xu, M.; Zhou, D.; Wu, T.; Qi, J.; Du, Q.; Xiao, Z. Self-Regulation of Spin Polarization Density Propelling the Ion Diffusion Kinetics for Flexible Potassium-Ion Batteries. *Adv. Funct. Mater.* **2022**, *32*, 2203263. [CrossRef]
43. Wang, J.; Guan, Y.; Zhang, Q.; Zhu, H.; Li, X.; Li, Y.; Dong, Z.; Yuan, G.; Cong, Y. Well-Dispersed Ultrafine Pt Nanoparticles Anchored on Oxygen-Rich Surface of V_2CT_x (MXene) for Boosting Hydrogen Evolution Reaction. *Appl. Surf. Sci.* **2022**, *582*, 152481. [CrossRef]
44. Chen, G.; Lv, J.; Han, Y.; Zhang, Q.; Liu, Y.; Lang, J.; Wu, X.; Wang, J.; Lu, M.; Zhang, J. Electron and Ion Transport Behavior of Vanadium Based MXene Induced by Pressure for Lithium Ion Intercalated Electrodes. *J. Colloid Interface Sci.* **2023**, *633*, 207–217. [CrossRef] [PubMed]
45. Wu, X.; Wang, H.; Zhao, Z.; Huang, B. Interstratification-Assembled 2D Black Phosphorene and V_2CT:X MXene as Superior Anodes for Boosting Potassium-Ion Storage. *J. Mater. Chem. A* **2020**, *8*, 12705–12715. [CrossRef]
46. Kim, Y.; Gkountaras, A.; Chaix-Pluchery, O.; Gélard, I.; Coraux, J.; Chapelier, C.; Barsoum, M.W.; Ouisse, T. Elementary Processes Governing V_2AlC Chemical Etching in HF. *RSC Adv.* **2020**, *10*, 25266–25274. [CrossRef]
47. Champagne, A.; Shi, L.; Ouisse, T.; Hackens, B.; Charlier, J.C. Electronic and Vibrational Properties of V_2C-Based MXenes: From Experiments to First-Principles Modeling. *Phys. Rev. B* **2018**, *97*, 115439. [CrossRef]
48. Melchior, S.A.; Raju, K.; Ike, I.S.; Erasmus, R.M.; Kabongo, G.; Sigalas, I.; Iyuke, S.E.; Ozoemena, K.I. High-Voltage Symmetric Supercapacitor Based on 2D Titanium Carbide (MXene, Ti_2CT_x)/Carbon Nanosphere Composites in a Neutral Aqueous Electrolyte. *J. Electrochem. Soc.* **2018**, *165*, A501–A511. [CrossRef]
49. Ureña-Begara, F.; Crunteanu, A.; Raskin, J.P. Raman and XPS Characterization of Vanadium Oxide Thin Films with Temperature. *Appl. Surf. Sci.* **2017**, *403*, 717–727. [CrossRef]
50. Shvets, P.; Dikaya, O.; Maksimova, K.; Goikhman, A. A Review of Raman Spectroscopy of Vanadium Oxides. *J. Raman Spectrosc.* **2019**, *50*, 1226–1244. [CrossRef]
51. Tolosa, A.; Fleischmann, S.; Grobelsek, I.; Presser, V. Electrospun Hybrid Vanadium Oxide/Carbon Fiber Mats for Lithium- and Sodium-Ion Battery Electrodes. *ACS Appl. Energy Mater.* **2018**, *1*, 3790–3801. [CrossRef]
52. Zhou, Y.; Ramanathan, S. GaN/VO_2 Heteroepitaxial p-n Junctions: Band Offset and Minority Carrier Dynamics. *J. Appl. Phys.* **2013**, *113*, 213703. [CrossRef]
53. Armer, C.F.; Lübke, M.; Johnson, I.; McColl, K.; Cora, F.; Yeoh, J.S.; Reddy, M.V.; Darr, J.A.; Li, X.; Lowe, A. Enhanced Electrochemical Performance of Electrospun V_2O_5 Fibres Doped with Redox-Inactive Metals. *J. Solid State Electrochem.* **2018**, *22*, 3703–3716. [CrossRef]
54. Mokrushin, A.S.; Fisenko, N.A.; Gorobtsov, P.Y.; Simonenko, T.L.; Simonenko, E.P.; Simonenko, N.P.; Glumov, O.V.; Melnikova, N.A.; Bukunov, K.A.; Sevastyanov, V.G.; et al. Pen Plotter Printing of ITO Thin Film as a Highly CO Sensitive Component of a Resistive Gas Sensor. *Talanta* **2021**, *221*, 121455. [CrossRef] [PubMed]
55. Simonenko, T.L.; Simonenko, N.P.; Gorobtsov, P.Y.; Mokrushin, A.S.; Solovey, V.R.; Pozharnitskaya, V.M.; Simonenko, E.P.; Glumov, O.V.; Melnikova, N.A.; Lizunova, A.A.; et al. Pen Plotter Printing of Co_3O_4 Thin Films: Features of the Microstructure, Optical, Electrophysical and Gas-Sensing Properties. *J. Alloys Compd.* **2020**, *832*, 154957. [CrossRef]
56. Nagornov, I.A.; Mokrushin, A.S.; Simonenko, E.P.; Simonenko, N.P.; Gorobtsov, P.Y.; Sevastyanov, V.G.; Kuznetsov, N.T. Zinc Oxide Obtained by the Solvothermal Method with High Sensitivity and Selectivity to Nitrogen Dioxide. *Ceram. Int.* **2020**, *46*, 7756–7766. [CrossRef]
57. Ji, H.; Zeng, W.; Li, Y. Gas Sensing Mechanisms of Metal Oxide Semiconductors: A Focus Review. *Nanoscale* **2019**, *11*, 22664–22684. [CrossRef]
58. Deng, Y. *Semiconducting Metal Oxides for Gas Sensing*; Elsivier: Amsterdam, The Netherlands, 2019; ISBN 9789811358524.

59. Degler, D.; Weimar, U.; Barsan, N. Current Understanding of the Fundamental Mechanisms of Doped and Loaded Semiconducting Metal-Oxide-Based Gas Sensing Materials. *ACS Sens.* **2019**, *4*, 2228–2249. [CrossRef]
60. Jeong, S.Y.; Kim, J.S.; Lee, J.H. Rational Design of Semiconductor-Based Chemiresistors and Their Libraries for Next-Generation Artificial Olfaction. *Adv. Mater.* **2020**, *32*, 2002075. [CrossRef]